Modeling of the Anode Crater Formation in Electrical Discharge Machining

Jia Tao

Jun Ni

Albert J. Shih

Department of Mechanical Engineering,
University of Michigan,
Ann Arbor, MI 48109

This research presents a numerical model and the experimental validation of the anode crater formation in electrical discharge machining (EDM) process. The modeling is based on the theory that the material removal process in EDM is composed of two consecutive phases: the plasma heating phase in which intensive thermal energy density is applied locally to melt the work-material and the bubble collapsing phase in which the fluidic impact expels the molten material. A mathematical heat source model with Gaussian distributed heat flux and time variant heating area is applied in the plasma heating phase. Standard modules of a commercial computational fluid dynamics software, FLUENT, *are adapted to model the crater formation in EDM. The material melting is simulated using transient heat transfer analysis and an enthalpy balance method. The volume of fraction (VOF) method is used to tackle the multiphase interactions in the processes of bubble compression and collapsing and molten material splashing and resolidification. Crater and debris geometries are attained from the model simulation and validation experiments are conducted to compare the crater morphology. The simulation and experiment results at different discharge conditions show good agreement on crater diameter suggest that the model is able to describe the mechanism of EDM crater formation.* [DOI: 10.1115/1.4005303]

1 Introduction

In electrical discharge machining (EDM), the material removal is realized by rapidly reoccurring electrical discharges. In an individual electrical discharge, the plasma channel exerts intensive thermal and power density on the discharge spot to induce the work-material melting and expulsion, and then leave a crater on the surface [1]. The consecutive discharges yield continual material removal and produce a machined surface composed of numerous overlapped discharge craters. This study aims to model the crater formation process, including the material melting, expulsion and resolidification during an individual electrical discharge. The model can provide insights to the material movement during the electrical discharge process.

The negative polarity, i.e., workpiece as anode, is usually used in EDM finishing process. The negative polarity setup produces low cathode electrode tool wear at short discharge duration ($<3\ \mu$s) [2] and smooth crater morphology on the anode surface [3]. Individual discharge craters are observed as dominant feature on the machined surface on anode in EDM finishing process. Even though both the anode and cathode experience rapid temperature rise and resultant material melting, they are found to have distinct material expulsion mechanisms and different crater morphologies [4]. An example is shown in Fig. 1. The model developed in this study will be able to estimate the anode material behavior in a discharge for the EDM finishing process.

The anode crater formation during electrical discharge is composed of two phases: plasma heating and bubble collapsing. The plasma heating phase starts after the dielectric fluid break-down with the formation of a plasma channel. The plasma heats the electrode with high thermal density, melts the anode material, and forms a melt pool [1]. The temperature at the center of the plasma channel measured by spectrometer is very high, ranging from 4000 to 8000 K [5]. The plasma channel is filled with gaseous mixture and expands as the discharge power input continues [6]. Together with the channel expansion, high pressure is built up inside the plasma channel. At the end of the discharge, the power input is ceased. The plasma, which is in the form of gaseous bubble, is compressed by the surrounding fluid and starts to collapse. The collapsing of the bubble exerts impact on the melt pool and causes the splashing of the molten liquid [1]. Some molten liquid is ejected into the surrounding dielectric fluid and flushed away. The remainder resolidifies and becomes part of a discharge crater.

Considerable studies have been conducted to model the plasma heating and material removal phases in a discharge. DiBitonto et al. [1] modeled the cathode material melting using a point heat source model. Patel et al. [7] proposed an expanding heat source model where a Gaussian distributed heat flux with time variant heating area was implemented as the heat source in melting the anode material. Eubank et al. [6] developed a variable mass model capable of calculating the temperature and pressure in a plasma bubble. The expanding heat source model [7] has been adopt in finite element analysis (FEA) to simulate the work-material melting, thermal stress, deformation and microstructure change caused by electrical discharge [8–11]. In this research, the expanding heat source model [7] is also adopted. The heat input can be applied to predict the melting of electrode- and work-material.

Shervani-Tabar et al. [12] conducted numerical analysis on the discharge bubble dynamics and showed the bubble was squeezed at the end of the discharge by the surrounding dielectric fluid and impinged on the melt pool. Hockenberry and Williams [13] experimentally studied the discharge bubble dynamics using a high-speed photography and suggested that the material removal was induced by the impingement of the liquid dielectric jets at the end of the discharge. Klocke et al. [14] measured the force of the discharge and concluded that the bubble collapsing created a dominating impact force. Eckman and Williams [15] theoretically derived the discharge bubble dynamics using the Navier–Stokes equation. Tohi et al. [16] measured the discharge force using the Hopkinson bar method and achieved good match with Eckman and Williams' theoretical results [15].

To the best of our knowledge, there is not yet a model incorporating both the plasma heating phase and the bubble collapsing phase to simulate the discharge crater formation. This study

Contributed by the Manufacturing Engineering Division of ASME for publication in the JOURNAL OF MANUFACTURING SCIENCE AND ENGINEERING. Manuscript received October 28, 2009; final manuscript received September 17, 2011; published online January 11, 2012. Assoc. Editor: Bin Wei.

Copyright © 2012 by ASME

Downloaded 11 Jan 2012 to 141.212.183.174. Redistribution subject to ASME license or copyright; see http://www.asme.org/terms/Terms_Use.cfm

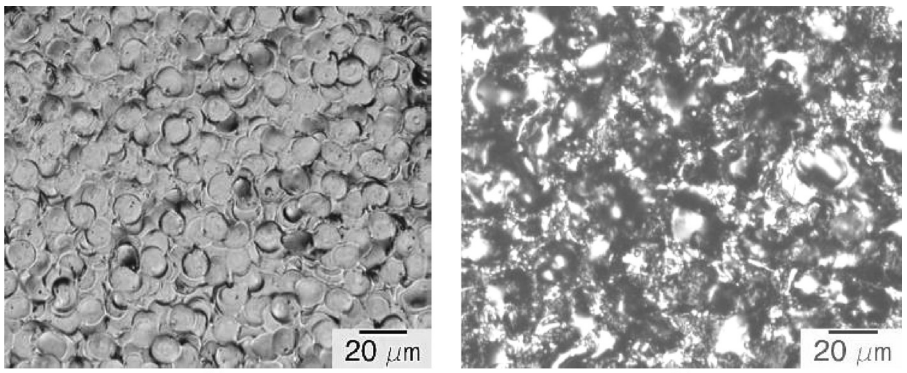

(a) (b)

Fig. 1 EDM surfaces of H13 tool steel with (*a*) negative polarity showing surface with clear feature of individual discharge craters (discharge current, $i_e = 1$ A, discharge duration $t_i = 0.5\ \mu$s, open circuit voltage and $u_i = 210$ V) (*b*) positive polarity showing rough surface with rugged features ($i_e = 2$ A, $t_i = 4\ \mu$s and $u_i = 210$ V) (electrode: copper)

develops a model that includes material melting, bubble compression and collapsing, and molten material splashing and resolidification. The model is constructed based on a commercial computational fluid dynamics software, FLUENT. For the plasma heating phase, the model can simulate the melting process and track the migrating melt fronts. The latent heat effect, which was not considered in previous research [7–10] and was first implemented by Lasagni et al. [11], is also included in this research. For the bubble collapsing phase, processes of multiphase interaction, liquid splashing and liquid–solid transformation are simulated to analyze the EDM material removal using the modules of volume of fraction (VOF) and melting and solidification in FLUENT. Das et al. [10] had similar attempt to model the material removal and they used a feature, called damage, in the commercial software, DEFORM, which is a mathematically defined quantity with preset threshold crossing which material failure is deemed and the element is removed from the model simulation. Their material removal is manually enforced depending on the mathematical expression of damage and its threshold setting, which was not discussed in detail in Ref. [10]. The present methodology is fundamentally different because it simulates the material removal in a more realistic manner, providing detailed information, including molten material protrusion, its interaction with surrounding dielectric fluid and debris formation, which are not available in Ref. [10].

The model is utilized to simulate and compare the discharge and crater formation in wet EDM with liquid kerosene and those in near-dry EDM with kerosene-air mixture dielectric fluid. Different levels of discharge pulse energy are also studied by the model. In the following sections, the modeling approach will be explained in detail. The simulation results will be presented and crater geometry is compared with experimental measurements. Parametric study on the bubble initial pressure is carried out to improve the model accuracy on crater geometry.

2 Modeling Approach

The modeling of the plasma heating phase and bubble collapsing phase is introduced in the following two sections.

2.1 Plasma Heating Phase

2.1.1 Energy Input. The energy for heating up the anode workpiece, E_a, comes from the discharge pulse energy, E_d, and is expressed as

$$E_a(t) = \eta E_d(t) = \eta \int_0^{t_i} i_e(t) u_e(t) dt \tag{1}$$

where i_e is the discharge current, u_e is the discharge voltage, t_i is the pulse duration, and η is the energy partition factor to the anode. In this study, $\eta = 0.39$ used by Yeo et al. [9] is utilized.

The power input for heating up the anode, $Q_a(t)$, can be expressed as

$$Q_a(t) = \eta i_e(t) u_e(t) \tag{2}$$

The i_e and u_e are experimentally measured. Three EDM finishing conditions, as shown in Fig. 2, are studied and are denoted as I, II, and III in descending order of their discharge energy.

2.1.2 Heat Flux Distribution. Based on the expanding heat source model [7], the heat flux has a Gaussian distribution in the plasma channel, as shown in Fig. 3. The time variant heat flux, $q_a(r, t)$, at a distance, r, from the center of the plasma column is expressed as

$$q_a(r,t) = q_{\max}(t) \exp\left[-3\left(\frac{r}{r_p(t)}\right)^2\right] \tag{3}$$

where $q_{\max}(t)$ is the maximum heat flux (at $r = 0$), $r_p(t)$ is the radius of the plasma heating area on the anode surface, and the exponential coefficient, -3, is selected from Murali and Yeo's study [8] where the micro-electrodischarge condition has energy levels very close to our study. Assuming a column-shaped plasma, $r_p(t)$ is equivalent to the radius of the plasma. $r_p(t)$ grows with time and is given by [7]

$$r_p = 0.788 t^{3/4} \tag{4}$$

The integration of the heat flux, $q_a(r, t)$, over the plasma heating area is the total power input for heating the anode, $Q_a(t)$

$$Q_a(t) = \int_0^{r_p} q_a(r,t) 2\pi r dr \tag{5}$$

Since $r_p(t)$ and $Q_a(t)$ are known for a specific time, t, $q_a(r, t)$ can be solved.

2.1.3 Model Schematics and Initial and Boundary Conditions. The axisymetric schematics of the model are shown in Fig. 4. The plasma heating phase modeling only includes the region of the anode workpiece, DFHG region in Fig. 4. The anode region is 100 and 80 μm along the r and z directions, respectively. This region is divided into 0.05 by 0.05 μm grids (cells).

Downloaded 11 Jan 2012 to 141.212.183.174. Redistribution subject to ASME license or copyright; see http://www.asme.org/terms/Terms_Use.cfm

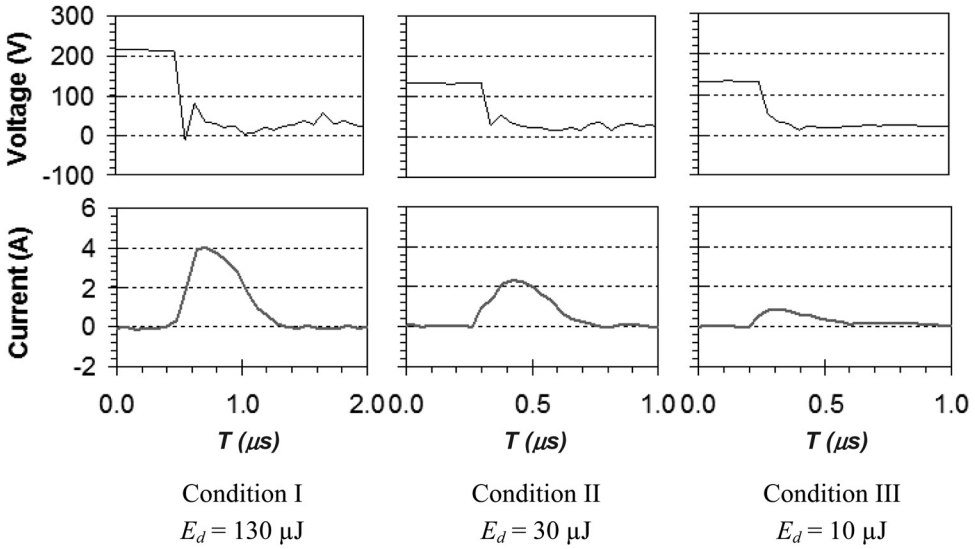

Fig. 2 Discharge waveforms of three experimentally measured discharge conditions

The initial temperature, T_i, of the workpiece is equal to the 300 K ambient temperature, T_0, at $t=0$ for the entire anode region.

At $t>0$, the heat source is applied on the anode surface, line DF. The heat flux boundary condition can be expressed as

$$z=0, \quad k\frac{\partial T}{\partial z}=\begin{cases} q_a(r,t), & \text{if } 0<r<r_p \\ 0, & \text{if } r>r_p \end{cases} \tag{6}$$

where k is the thermal conductivity of the workpiece material. The boundary condition at lines FH and GH (see Fig. 4) away from the discharge region is assumed at a constant temperature T_0.

2.1.4 Melting and Solidification. The melting and solidification module in FLUENT is utilized to simulate the rapid heating and cooling of the material during a discharge. The enthalpy-porosity method [17] is applied to tackle the energy balance and viscosity change in the melting process. The melt interface is not tracked explicitly. Instead, a quantity called the liquid fraction, β, which indicates the fraction of the cell volume that is in liquid form, is computed based on an enthalpy balance. The total enthalpy of the material, H, is composed of the sensible enthalpy, h, induced by the material temperature change, and the latent heat, ΔH, induced by the phase change

$$H=h+\Delta H \tag{7}$$

$$h=h_{\text{ref}}+\int_{T_{\text{ref}}}^{T} C_p dT \tag{8}$$

$$\Delta H=\beta L \tag{9}$$

where h_{ref} is the reference enthalpy, T_{ref} is the reference temperature, C_p is the specific heat at constant pressure, L is the latent heat of the material, and β is the liquid fraction. The work-material, AISI H13 tool steel, is an alloy material. The melting involves the mushy zone [17] and β can be expressed as

$$\beta=\begin{cases} 0, T<T_{\text{solidus}} \\ \dfrac{T-T_{\text{solidus}}}{T_{\text{liquidus}}-T_{\text{solidus}}}, T_{\text{solidus}}<T<T_{\text{liquidus}} \\ 1, T>T_{\text{liquidus}} \end{cases} \tag{10}$$

2.1.5 Material Properties. Tables 1 and 2 summarize the material properties of H13 tool steel. For the temperature-dependant properties, the linear interpolation is applied at the temperature level that is not prescribed by the tables.

2.2 Bubble Collapsing Phase

2.2.1 Model Schematics and Initial and Boundary Conditions. Figure 4 shows the axisymetric schematics of the bubble collapsing model. In addition to the anode region DFHG

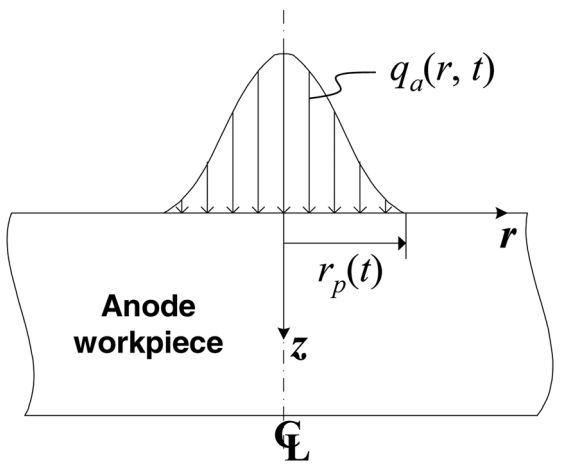

Fig. 3 Profile of Gaussian distributed heat flux

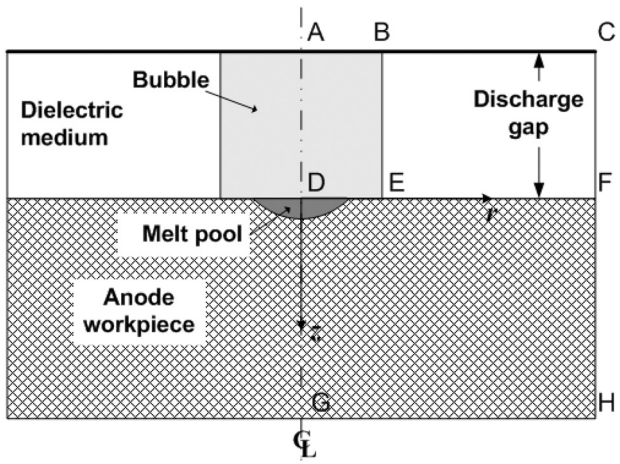

Fig. 4 Schematics of the bubble collapsing model

Downloaded 11 Jan 2012 to 141.212.183.174. Redistribution subject to ASME license or copyright; see http://www.asme.org/terms/Terms_Use.cfm

Table 1 Properties of AISI H13 tool steel [18,19]

Nomenclature	Symbol	Unit	Value
Solid density	ρ_s	kg/m^3	7760
Liquid density	ρ_l	kg/m^3	7000
Solid heat capacitance	C_{p-s}	J/kg K	460
Liquid heat capacitance	C_{p-l}	J/kg K	480
Latent heat of melting	L_{-h}	kJ/kg	250
Solidus temperature	T_s	K	1634
Liquidus temperature	T_l	K	1744
Dynamic viscosity of molten material	μ	(kg/m s)	0.006
Surface tension coefficient	Γ	N/m	1.9

modeled in the plasma heating phase, the bubble (region ABDE), cathode surface (line AC), and dielectric fluid (region BCFE) are also included in the model. The same 0.05 μm square grid (cell) as in the anode region is applied.

As part of the initial conditions for the bubble collapsing phase, the temperature profile, and melt pool geometry in the anode region DFHG are imported from the plasma heating phase. The cathode, line AC, is simplified as a rigid and adiabatic boundary with the same temperature distribution as that on the anode surface (line DF). The vertical distance between the cathode and anode surfaces, i.e., the discharge gap distance in Fig. 4, is 20 μm and is determined experimentally by measuring the actual depth of cut and tool wear of the die-sinking EDM. The variation is less than 10% for all the investigated discharge conditions.

The column-shape bubble, region ABED, is adjacent to the anode melt pool. The initial radius of the bubble is equal to the plasma radius at the end of the plasma heating phase, which is determined by Eq. (4). The bubble is filled with kerosene vapor, which is modeled as compressible ideal gas with properties listed in Table 3.

The initial temperature in the bubble is set at 5000 K [5]. The initial bubble pressure of 200 MPa, which falls into the estimated range according to the previous studies [6,15], is used in the first set of simulations. Since large variation is encountered in the bubble pressure estimation [6,15], the second set of simulations study the effect of initial bubble pressure at four levels, 20 MPa, 200 MPa, 2 GPa, and 20 GPa, on the crater geometry.

The region BCFE is filled with dielectric fluid. Liquid kerosene and kerosene-air mixture (20% kerosene and 80% air [21]) are used for the wet and near-dry EDM simulations, respectively. Both liquid kerosene and kerosene-air mixture are modeled as incompressible phase and properties are in Table 3. The initial temperature in the dielectric fluid region is assumed to have an exponential decaying distribution. At the bubble and dielectric fluid interface (line BE), 5000 K is assigned to the dielectric fluid and it exponentially drops to the ambient temperature, 300 K, at the boundary line CF. The exponential temperature distribution in dielectric fluid is hypothesized as an exponential temperature distribution is observed on the anode material at the end of the plasma heating phase. Even though Lasagni et al. [11] assumed that the ambient temperature occurred at an infinite distance away from the heat source, the 100 μm distribution distance is considered appropriate for current study because the simulation does not yield significant difference when extending the simulation region beyond 100 μm. In fact, since the contacting metal electrode 40 μm away from the heat source is at ambient temperature and of high thermal conductivity, any temperature differential between the dielectric fluid and electrode is brought to equilibrium, around ambient temperature, immediately after the simulation starts. Therefore, for the sake of computation efficiency, the distribution distance is set at 100 μm which is an approximation but manages to yield reasonable results. The boundary line CF is set as a pressure inlet with the flow direction perpendicular to the line CF. The initial pressure of boundary CF is set equal to the initial bubble pressure and is assumed to decay exponentially with a time constant of 10^{-8} s once the bubble is collapsed.

Table 2 Temperature-dependent thermal conductivity for AISI H13 tool steel [20]

Temperature(K)	k(W/m K)
300	28.6
488	28.6
623	28.4
748	28.4
878	28.7

2.2.2 VOF Modeling. Since five phases, kerosene vapor, air, kerosene liquid, molten steel and solid steel co-exist in the bubble collapsing model, the VOF module is applied to analyze their interactions. The VOF models immiscible fluids (or phases) by solving a set of momentum equations and tracking the volume fraction of each of the phases [17]. The five phases are not interpenetrating in the model. For each phase, q, in the model, a variable, a_q, the phase volume fraction in the computational cell, is assigned to the phase. The volume fraction of phase q in the cell can be described by one of the following three conditions:

$a_q = 0$, if the cell is empty of phase q;

$a_q = 1$, if the cell is full of phase q;

$0 < a_q < 1$, if the cell contains the interface between phase q and one or more other phases.

Based on the local value of a_q, the properties, such as density, ρ, and viscosity, μ, of the cell are approximated with a volume-averaged manner [17], i.e.,

$$\rho = \sum a_q \rho_q \tag{11}$$

$$\mu = \sum a_q \mu_q \tag{12}$$

The momentum equation is solved throughout the computational cell, and the resulting velocity vector, $\vec{v}$, is shared among the phases. The momentum equation is dependant on the volume-averaged density, ρ, and viscosity, μ, within the cell. The moment equation is [17]

$$\frac{\partial}{\partial t}\left(\rho\vec{v}\right) + \nabla \cdot \left(\rho\vec{v}\vec{v}\right) = -\nabla p + \nabla \cdot \left[\mu\left(\nabla\vec{v} + \nabla\vec{v}^T\right)\right] + \rho\vec{g} + \vec{F} \tag{13}$$

Table 3 Properties of kerosene vapor and kerosene liquid [17]

			Bubble	Dielectric fluid	
Model parameter	Symbol	Unit	Kerosene vapor	Kerosene	Air
Density	ρ	kg/m^3	Follow ideal gas law	780	1.23
Molecular weight	m	kg/mol	167	167	29.0
Heat capacitance	C_p	J/kg K	460	2090	1006
Thermal conductivity	k	(W/m K)	0.018	0.149	0.024
Dynamic viscosity	μ	(kg/m s)	7.0×10^{-6}	0.0024	1.8×10^{-5}

Downloaded 11 Jan 2012 to 141.212.183.174. Redistribution subject to ASME license or copyright; see http://www.asme.org/terms/Terms_Use.cfm

where p is the pressure at the center of the cell, $\vec{g}$ is the gravitational acceleration and $\vec{F}$ is the volumetric force.

The energy equation is solved with the velocity vector also shared among the phases [17]

$$\frac{\partial}{\partial t}(\rho E) + \nabla \cdot \left(\vec{v}(\rho E + p)\right) = \nabla \cdot (k_{\text{eff}} \nabla T) + S_h \tag{14}$$

where k_{eff} is the volume-averaged effective thermal conductivity and S_{h} is the volumetric heat sources. The energy, E, and temperature, T, are treated as mass-averaged variables [17]

$$E = \frac{\Sigma \alpha_q \rho_q E_q}{\Sigma \alpha_q \rho_q} \tag{15}$$

$$T = \frac{\Sigma \alpha_q \rho_q T_q}{\Sigma \alpha_q \rho_q} \tag{16}$$

2.2.3 Liquid, Solid, and Mushy Region Modeling. Additional effort is needed to model the phases of liquid, solid and mushy zone, which co-exist at the alloy melting stage. It is difficult to incorporate both fluid and solid together in the same analysis domain since they are constructed with different principles. In this study, both liquid and solid phases are modeled using fluid type cell. Methods of temperature-dependant viscosity proposed by Li et al. [22] and enthalpy-porosity technique built in FLUENT [17] are adopted to make the modeling of solid phase possible. In the temperature-dependant viscosity method, the element of temperature lower than the solidus temperature is assigned a very high viscosity (100–2000 N s/m depending on the simulation stability) to mimic the solid status. In this way, the flow or movement of the solid work-material is very small and its influence on the modeling accuracy is limited. If the material temperature is higher than the liquidus temperature, the material is in the liquid phase and the viscosity value listed in Table 1 is assigned.

Between the solidus and liquidus temperatures, i.e., in the mushy zone, an intermediate viscosity could be used to simulate the solidus status. FLUENT's enthalpy-porosity method is more effective to handle the transition between liquid and solid. It treats the mushy region as a porous medium [17]. The porosity is set equal to the liquid fraction in that cell. Thus, higher portion of the liquid fraction induces less stagnancy to dissipate the momentum of the fluid flow, i.e., the relative motion between the liquid and solid in the mushy zone. The momentum dissipation, $\vec{M}_{\text{d}}$, in the mushy zone is [17]

$$(\vec{M}_d = \frac{(1-\beta)^2}{(\beta^3 + \varepsilon)} A_{\text{mush}} (\vec{v} - \vec{v}_p) \tag{17}$$

where β is the liquid fraction, ε is a small number to prevent division by zero for fully solidified case, $\vec{v}_p$ is the vector of solid velocity due to entire movement of the domain, and A_{mush} is the dimensionless mushy zone constant. Higher A_{mush} causes large energy dissipation. In this study, A_{mush} equals to 10^7 [17] is used.

3 Simulation Results

3.2 Plasma Heating Phase. Figure 5 shows the simulation results of the temperature distribution on the anode work-material and solid fraction during the 0.5 μs plasma heating phase in discharge condition III (Fig. 2). It is observed that the heated area on the anode increases with the duration of the plasma heating. The peak temperature reaches 10900 K at 0.1 μs and drops to 3400 K at 0.5 μs. The drop of the peak temperature is mainly due to the expansion of the plasma channel, which reduces the discharge power density, and the dissipation of energy to the surrounding area.

The second row of plots in Figure 5 shows the solid fraction of the work-material representing its melting and solidification status. At the start (0.0 μs), the anode work-material (bottom portion in Fig. 5) has 100% solid phase. The upper portion is the nonsolid phase, which can contain both the molten liquid and other liquid phases, including the bubble and surrounding dielectric fluid. There is a thin transition band between the solid and liquid phases used in FLUENT to avoid abrupt change of phases and the associated

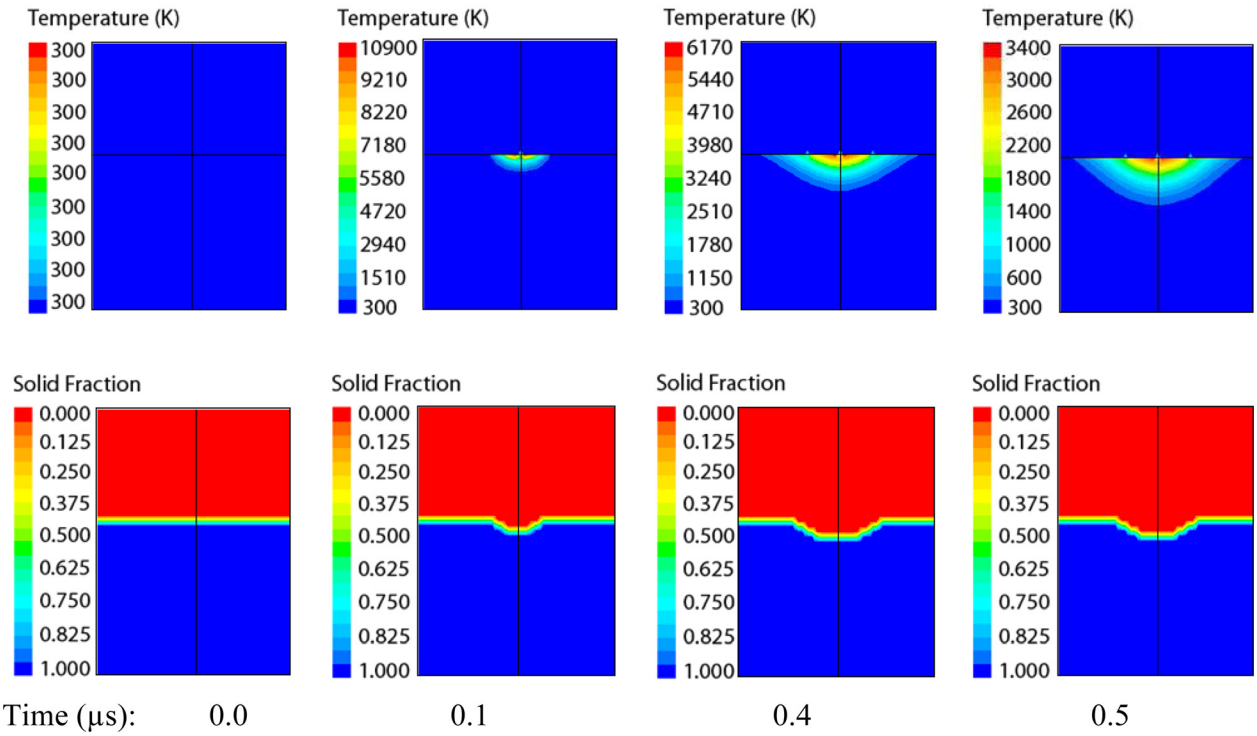

Fig. 5 Simulation of the plasma heating phase

Downloaded 11 Jan 2012 to 141.212.183.174. Redistribution subject to ASME license or copyright; see http://www.asme.org/terms/Terms_Use.cfm

computational problem. The transition band, about 1 μm thick, exists in all diagrams of phase fraction results. As the temperature rises, the anode workpiece starts to melt and a cavity formed on top indicates the formation of melt pool. The size of melt pool reaches the maximum at about 0.4 μs. After that, the growth stops. The size of melt pool at 0.5 μs is slightly smaller than that at 0.4 μs. This is related to the temperature drop during the plasma heating phase. The expansion of the plasma channel reduces the heating power density to such a level that the heat dissipation, mainly induced by conduction, surpasses the thermal input. The shrinkage of melt pool size during the plasma heating phase is a waste of discharge energy. Therefore, the modeling of plasma heating phase can potentially be applied to optimize the discharge power and duration to improve the material removal rate and energy efficiency.

3.3 Bubble Collapsing Phase. Figure 6 shows the simulation results of the bubble collapsing phase in wet EDM of discharge condition III. The plots of bubble fraction, work-material fraction and solid fraction are displayed at simulation time steps of 0.0, 0.12, 0.22, 0.32, 0.42, and 0.52 μs to describe the crater formation process.

As shown in the bubble fraction, the initial bubble column is 15 μm in diameter and 20 μm in height at 0.0 s. The bubble is compressed rapidly due to the quick temperature drop and the high pressure of the surrounding dielectric fluid. At 0.12 μs, the bubble is compressed to less than 5 μm in diameter. The bubble collapses at around 0.22 μs when the dielectric fluid penetrates the bubble and breaks it into small pieces. The collapsing of bubble exerts an impact on the melt pool and causes splashing of the molten work-material.

In the plots of the work-material fraction, the bottom portion represents the anode work-material. At 0.12 μs, before the collapsing of the bubble, the molten part of the work-material deforms slightly. At 0.22 μs, as the bubble collapses, the impact causes a dimple at the center of the melt pool. The molten liquid is agitated and displaced toward the side of the melt pool at 0.32 μs. Part of the material starts to detach from the melt pool at 0.42 μs. The detached material solidifies into small droplets and becomes ejected debris particles. The remainder molten material does not attain enough momentum from the impact, resolidifies, and becomes the crater and part of the recast layer on the EDM surface.

In the plots of the solid fraction, the bottom portion is the solid (unmelt) work-material and a cavity of the melt pool in liquid phase can be identified. Before the bubble collapsing at 0.22 μs, solidification of the molten pool is observed from the reduction of the cavity size. The impact induced by the bubble collapsing displaces the molten material and induces strong convection in the melt pool. The ejected molten material starts to solidify at 0.32 μs and becomes debris droplet at 0.42 μs. The final formation of the crater is at 0.52 μs when the profiles of the work-material fraction and solid fraction become identical indicating the complete solidification of the molten material.

3.4 Crater Formation Simulation. The crater geometry, represented by the work-material fraction after the material solidification for near-dry and wet EDM under discharge conditions I, II, and III, is shown in Fig. 7. The initial bubble pressure was set at 2×10^8 Pa. The predicted crater geometry will be compared to the experimentally measured craters for model validation.

Corresponding to discharge conditions I, II, III, the crater diameter is estimated to be 23.0, 13.4, and 11.0 μm for near-dry EDM and 20.1, 13.2, and 10.5 μm for wet EDM, respectively. In general, the near-dry EDM has slightly larger crater diameter than that of the wet EDM. The opposite trend is observed for the crater depth, i.e., near-dry EDM has shallower crater depth than that of wet EDM. The crater geometry is affected by density, viscosity, and thermal conductivity of the dielectric fluid. The high density and viscosity of the kerosene liquid in wet EDM yields larger momentum when compressing the bubble and causes stronger impact at the bubble collapsing. The molten material is agitated and ejected deeper from the molten pool; therefore, the crater is deeper and has smaller diameter in the wet EDM.

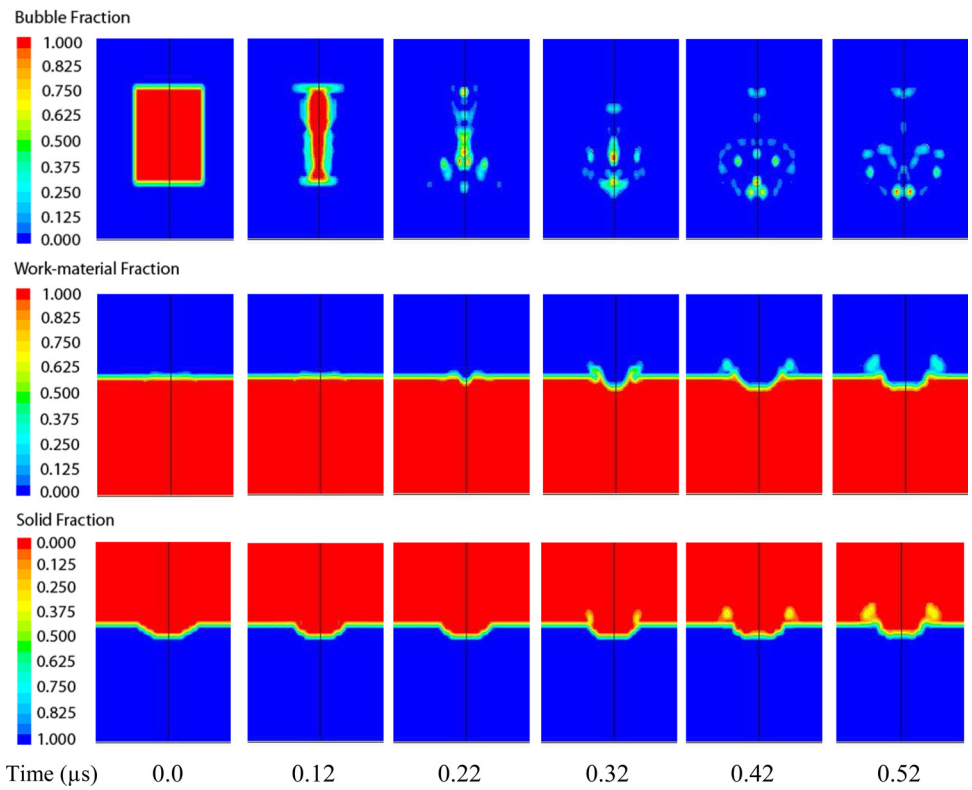

Fig. 6 Simulated bubble collapsing phase in wet EDM under discharge Condition III

Downloaded 11 Jan 2012 to 141.212.183.174. Redistribution subject to ASME license or copyright; see http://www.asme.org/terms/Terms_Use.cfm

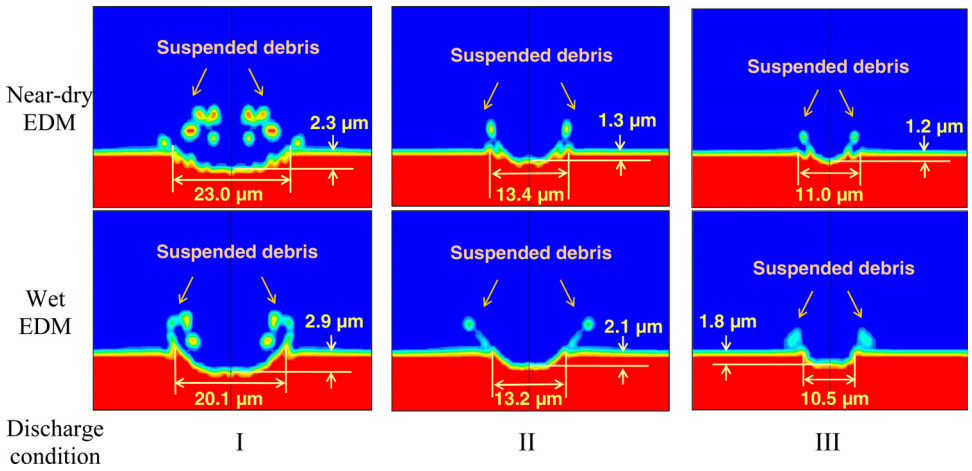

Fig. 7 Simulated work-material fraction for near-dry and wet EDM craters under discharge conditions I, II, and III

The crater diameter and depth is observed to reduce with the decrease of discharge energy in discharge conditions I–III. With lower discharge energy to melt less material, a smaller size of the melt pool is generated and the size of the final crater is reduced.

4 Experimental Crater Generation and Measurement

Experiments were performed to create discharge craters. The size and shape of the crater are measured using an atomic force microscope (AFM) (NanoScope IIIa) with a J-type scanner head at tapping mode, 0.4 Hz scanning rate and 0.07 μm resolution. The measured crater geometry is compared with the model prediction.

Discharge craters can be generated under different discharge conditions. The EDM process creates overlapping craters, as illustrated in Fig. 1(*a*), and it is difficult to accurately measure individual crater geometry. A single discharge process can be utilized [23,24] but the discharge gap is small [23] which is different from that in the actual EDM process. A new method called sparsely continual discharge (SCD) is used.

In SCD, the workpiece is first polished to a mirror finish to make sure the small discharge craters can be distinguished from the original surface. For a 10 mm × 10 mm area with H13 anode work-material and copper electrode, the discharge gap distance is around 20 μm, which is the same as the gap distance in the continual discharge condition. The discharge condition is preset and controlled by the EDM machine (Sodick Model Model AQ55L) and the discharge wave form is monitored using oscilloscope (Agilent Infiniium 54833 A digital oscilloscope) connected directly to the electrodes. The discharges are reasonably consistent to the preset output on i_e, u_e, and t_i. After about 2–3 s of discharge, a cluster of sparsely distributed craters can be observed on the surface for analysis. Figure 8 shows an example of the crater cluster for near-dry EDM using discharge condition II. Craters with reasonable consistency in size and shape are attained. Since minority of abnormal discharges and craters can be easily distinguished and excluded from analysis, an arbitrary normal discharge waveform and crater is used for analysis, which we consider is representative thanks to the high consistency of the discharge pulse and crater geometry.

Figure 9 shows the optical micrograph, AFM 3D image, and cross section of craters generated under wet and near-dry EDM with discharge conditions I, II, and III. The optical micrograph and AFM 3D image are for visual assessment of the crater morphology. The crater cross section is obtained from AFM data and applied to measure the crater diameter and depth.

As seen in Fig. 9, from conditions I to III, the crater size reduces with the decrease of the discharge energy. When the discharge energy is 130, 30, and 10 μJ, the crater diameter is around 20, 13, and 10 μm and the peak crater depth is around 2.0, 0.4, and 0.1 μm, respectively. From condition I to conditions II and III, the reduction of the crater depth is significant. For crater under discharge conditions II and III, a bulged bottom is observed at the center of the crater. It is most obvious for the crater generated by near-dry EDM with condition II and can be identified simply from the 3D image. The cross section profiles show that a similar bulged bottom exists in discharge conditions II and III. For condition III, the bulged center can even raise above the original surface level causing a slightly negative depth. This is effective to make a flattened crater and achieve fine surface finish on the machined surface in EDM finish machining.

The melt pool is considered to burst from the center and the molten material is pushed toward the edge of the pool. Portion of the molten material solidifies on the edge forming a crest 0.1–0.5 μm above the original level surface. The solidified crater

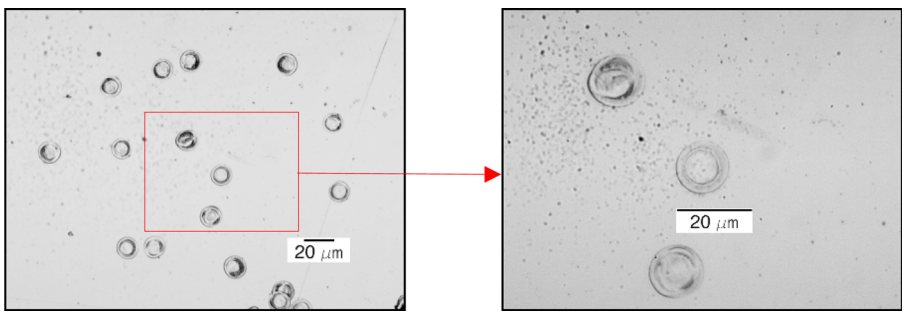

Fig. 8 Discharge craters generated by continual discharge process (near-dry EDM with discharge condition II)

Downloaded 11 Jan 2012 to 141.212.183.174. Redistribution subject to ASME license or copyright; see http://www.asme.org/terms/Terms_Use.cfm

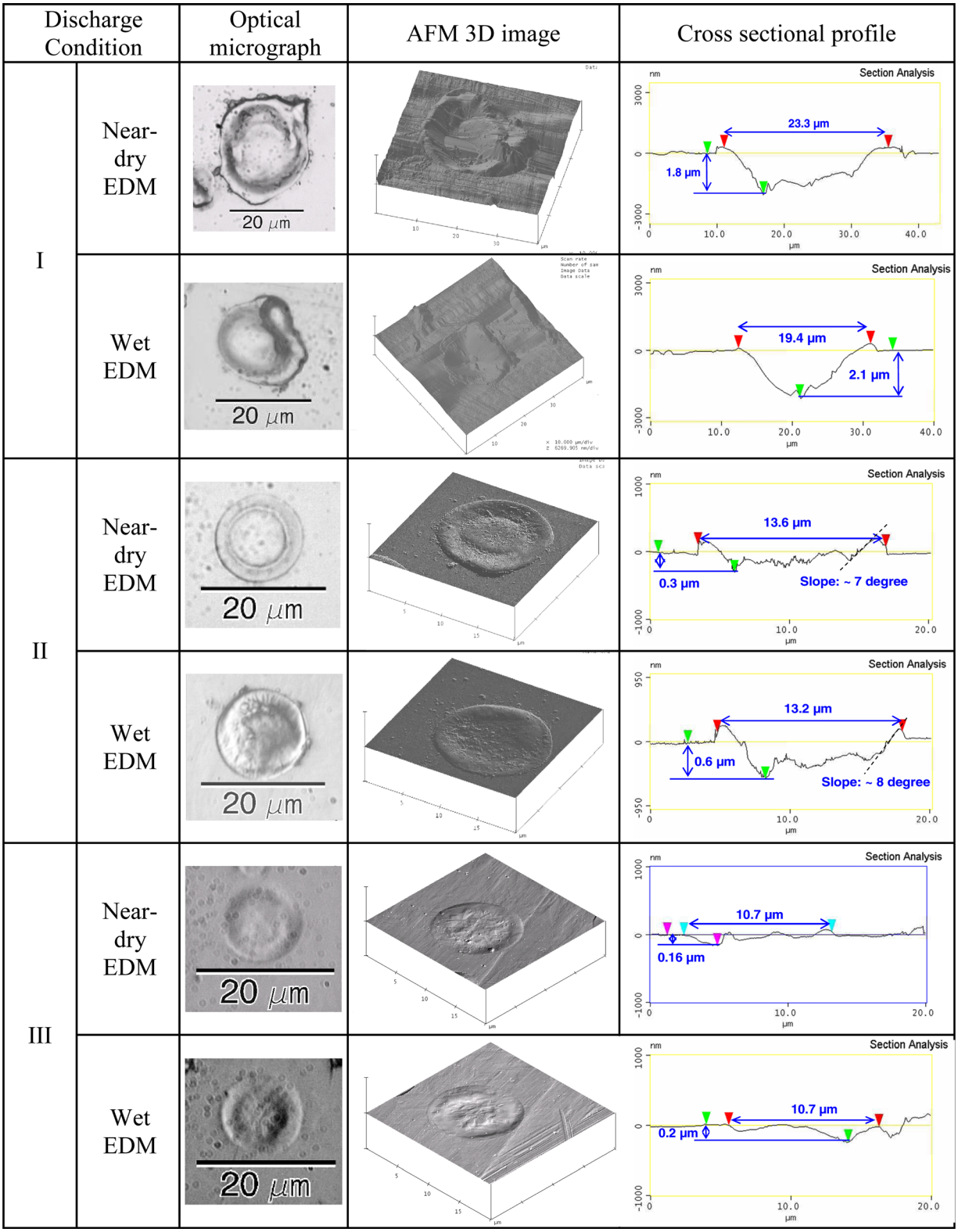

Fig. 9 Experimental craters under six EDM conditions

center is quite smooth as a consequence of the surface tension of the molten liquid.

Wet and near-dry EDM processes generate different crater, especially in the high discharge energy case, condition I. The near-dry EDM crater has larger diameter (23 μm versus 18 μm) and smaller depth (1.8 μm versus 2.3 μm). Under the same EDM condition, a relatively flat crater is created in near-dry EDM, which is more suitable for finishing EDM [25]. The crater diameter and depth are related to different dielectric fluid properties. The kerosene-air mixture used in near-dry EDM has lower viscosity and density because of the dilution by air. It generates less momentum when compressing the bubble and consequently smaller bubble collapsing impact force.

Downloaded 11 Jan 2012 to 141.212.183.174. Redistribution subject to ASME license or copyright; see http://www.asme.org/terms/Terms_Use.cfm

As the pulse energy decreases, the differences in crater geometry between the near-dry and wet EDM become less obvious. For condition II, the crater generated by near-dry EDM is slightly shallower, around 0.3 μm, in depth. No significant difference of crater geometry is observed between near-dry and wet EDM for condition III. The smaller discharge energy reduces the bubble collapsing impact force. The molten material thus attains less momentum to overcome the surface tension of the melt pool. As the surface tension plays a larger role, the effect of impact force on material removal becomes less significant, which diminishes the difference of crater geometry between wet and near-dry EDM when the pulse energy is reduced.

5 Comparison and Discussion

Figure 10 compares the diameter and depth of the model predicted and experimentally measured discharge craters. The model provides good prediction on the crater diameter with less than 10% deviation from the mean value of the experiments for all six discharge conditions. It captures characteristics of actual crater formation. Both modeled and real craters in Figs. 8 and 9, respectively, show features of ridge and bulged crater bottom. The model distinguishes the craters generated by near-dry and wet EDM and predicts the trend of decreasing crater size with the reduction of discharge energy. However, the model is not able to accurately estimate the shallow crater depth in conditions II and III.

The model tends to overestimate the crater depth. For condition I, which has relatively high pulse energy, 130 μJ, the simulated crater depth is in the upper range of experimental variation. As the discharge energy drops to 30 and 10 μJ for conditions II and III, respectively, the experimentally measured crater depth reduces to less than 1 μm and some bulged part of the crater even rises above the original surface level. In these cases, the simulated craters are all deeper than 1.2 μm.

The overestimation of the crater depth can be attributed to several reasons. First, the specific volume of the solidified metal can increase, i.e., the material volume expands, if the cooling rate exceeds a critical value [26]. The cooling rate encountered during the discharge crater formation is higher than 10^9 K/s as estimated by the simulation. This rapid cooling rate has surpassed the critical value, generally 10^5 K/s [26], for metallic alloys. The steel work-material is thus expected to expand during solidification after the discharge. The expanded volume occupies more space in the crater and reduces the crater depth.

Second, the plasma heating phase model probably overestimates the melt pool depth in the first part of the simulation. The actual melt pool depth can be roughly estimated by summing up the measured crater depth and the recast layer thickness. The measured crater depth is less than 0.9 and 0.4 μm for conditions II and III, respectively. The recast layer thickness measured after continual EDM is generally less than 1.7 and 1.5 μm in conditions II and III, respectively, although there is a possibility of overestimation due to overlapping of multiple recast layers in continual EDM. The deduced actual melt pool depth is 2.6 and 1.9 μm for conditions II and III, respectively, which is still smaller than the simulation results (2.7 and 2.2 μm for conditions II and III, respectively). Therefore, a more accurate plasma heating phase model is needed to fit the specific condition of low discharge energy level (less than 100 μJ).

Third, the initial bubble pressure in the simulation may not be accurate. In the simulation, the initial bubble pressure was 2×10^8 Pa for all discharge conditions. Since the build-up of the bubble pressure is related to the discharge pulse energy, the actual pressure will vary. Higher energy is expected to expand the bubble more violently, resulting in a higher initial bubble pressure and consequently stronger compression at the end of the discharge. To overcome the absence of accurate bubble pressure, a study is conducted in the next section to investigate the effect of initial bubble pressure on the crater formation.

6 Effect of Initial Bubble Pressure

The simulation is conducted at four levels of initial bubble pressure, 2×10^7, 2×10^8, 2×10^9, and 2×10^{10} Pa, in near-dry EDM with discharge conditions I, II, and III. Results are shown in Fig. 11.

In Fig. 11, the simulated crater diameter increases with the rise of the initial bubble pressure. For conditions I, II, and III, when the initial bubble pressure is increased from 2×10^7 to 2×10^{10} Pa, the percentages of crater diameter and depth increases are 14%, 9% and 5% and 26%, 50%, and 30%, respectively. The variation of initial bubble pressure has a larger effect on the crater depth. Also, the material ejection appears more violent in the high pressure case with wider spread debris droplets.

Comparing the simulated and real craters, the initial bubble pressure of 2×10^8 Pa provides the closest prediction on crater diameter and depth for conditions I and II. For condition III, the pressure of 2×10^7 Pa yields a good match in the simulated and real crater profiles (Fig. 9, near-dry EDM with condition III). In

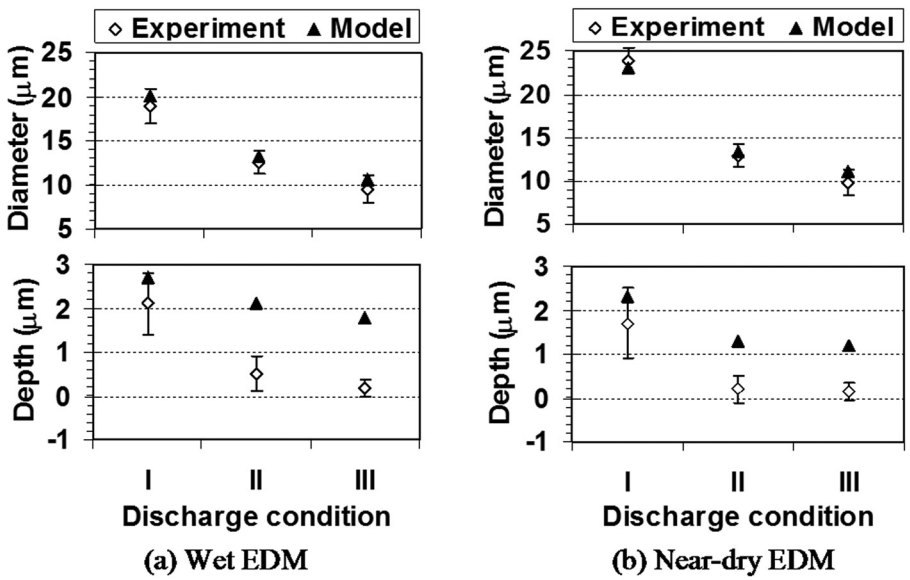

Fig. 10 Dimensional comparison of experimental and simulated craters

Downloaded 11 Jan 2012 to 141.212.183.174. Redistribution subject to ASME license or copyright; see http://www.asme.org/terms/Terms_Use.cfm

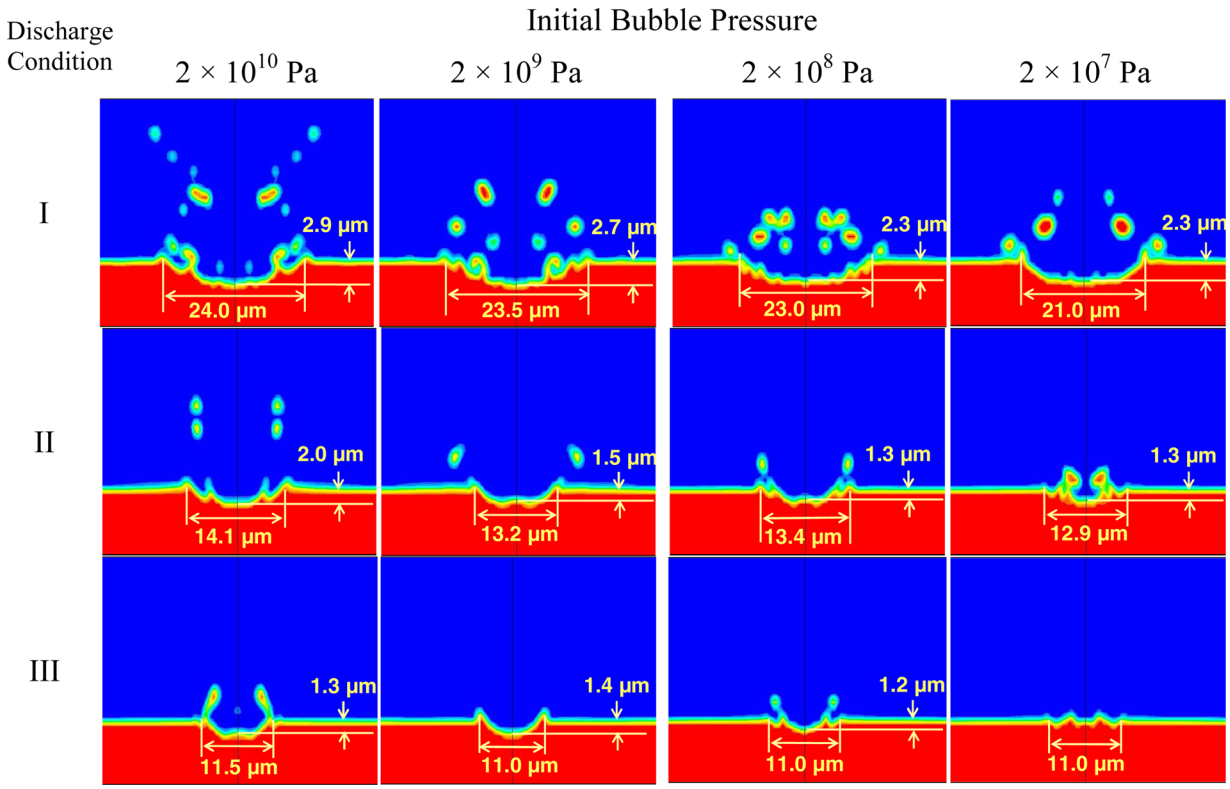

Fig. 11 Effect of initial bubble pressure in near-dry EDM on crater geometry in three discharge conditions

both profiles, the periphery slightly slides downward while the center bulges up and rises above the original surface level. No material ejection happens in that simulation.

The prediction of the crater depth does not improve by varying the initial bubble pressure in discharge conditions I and II. The bubble pressure is not a major factor for the crater depth overestimation by the model. The other two factors, material volume expansion and overestimation of the melt pool depth, discussed in Sec. 5 are inferred as the major problems that should be solved to improve the model accuracy.

The model improvement can be expected as follows. First, model parameters in the plasma heating phase, which have used the literature values in the current study, should be revised to better fit the low discharge energy (less than 100 μJ) case. Second, the factor of material expansion at high cooling rate needs to be included by implementing an empirical data base correlating the change of material specific volume with its cooling rate. Also, another potential advancement is to incorporate the modeling of bubble expansion. With that, a more accurate bubble pressure can be utilized instead of using the literatures values. The challenge is that the bubble expansion modeling requires two compressible flows, one for vapor bubble and the other for surrounding dielectric fluid. Currently, this condition is not possible for FLUENT and other CFD software.

7 Concluding Remarks

This study has developed a model for the discharge crater formation on anode electrode. Advancing based on the plasma heating model [7], the model developed here can handle the material melting and solidification by taking the latent heat into consideration. This model further incorporated the bubble collapsing phase to simulate the multiphase interactions among dielectric fluid, bubble, molten material, and solid workpiece. The modeling of discharge crater formation process using FLUENT software was proven feasible by comparing with experimentally measured crater diameter and depth.

The experimental validation was conducted using sparsely continual discharge which can better imitate the practical EDM process. The simulation generated realistic crater morphology, such as build-up crest and bulged bottom. The model provided good prediction on the crater diameter. Both the experiment and simulation suggested that the near-dry EDM using kerosene-air generates larger but shallower discharge craters than wet EDM using liquid kerosene. The model traced the trend of reducing crater size with the decrease of discharge energy. The initial bulb pressure influenced the simulation accuracy to some extent. The initial bubble pressure ranging from 10^7 to 10^8 Pa was found appropriate to simulate the crater geometry that can match with the experiments. Lower initial bubble pressure was found associated with the lower discharge pulse energy.

The model was found to overestimate the crater depth. The reason was identified as the inaccurate initial bubble pressure input, the overestimation of the melt pool depth and the ignorance of the material volume expansion under high cooling rate. The model could be improved by revising the plasma heating phase model to better estimate the melt pool size and by incorporating the cooling rate effect on the material specific volume.

Acknowledgment

This research is sponsored by the NIST Advanced Technology Program. Discussion with Dr. Yuefeng Luo of Federal Mogul is greatly appreciated.

References

[1] DiBitonto, D. D., Eubank, P. T., Patel, M. R., and Barrufet, M. A., 1989, "Theoretical Models of the Electrical Discharge Machining Process. I. A simple Cathode Erosion Model," J. Appl. Phys., **66**, pp. 4095–4103.
[2] Arunachalam, C., 1995, "Modeling the Electrical Discharge Machining Process," Ph.D. thesis, Texas A&M University, 4.
[3] Tamura, T., and Kobayashi, Y., 2004, "Measurement of Impulsive Forces and Crater Formation in Impulse Discharge," J. Mater. Process Tech., **149**, pp. 212–216.
[4] Luo, Y. F., and Tao, J., 2009 "Metal Removal in EDM Driven by Shifting Secondary Discharge," J. Manuf. Sci. Eng., **131**, 031014.

Downloaded 11 Jan 2012 to 141.212.183.174. Redistribution subject to ASME license or copyright; see http://www.asme.org/terms/Terms_Use.cfm

[5] Natsu, W., Ojima, S., Kobayashi, T., and Kunieda, M., 2004, "Temperature Distribution Measurement in EDM Arc Plasma Using Spectroscopy," JSME Int. J., Ser. C, **47**, pp. 384–390.
[6] Eubank, P. T., Patel, M. R., Burrufet, M. A., and Bozkurt, B., 1993, "Theoretical Models of the Electrical Discharge Machining Process. III. The Variable Mass, Cylindrical Plasma Model," J. Appl. Phys., **73**, 7900–7909.
[7] Patel, M. R., Barrufet, M. A., Eubank, P. T., and DiBitonto, D. D., 1989 "Theoretical Models of the Electrical Discharge Machining Process. II. The Anode Erosion Model," J. Appl. Phys., **66**, pp. 4104–4111.
[8] Murali, M. S., and Yeo, S. H., 2005, "Process Simulation and Residual Stress Estimation of Micro-Electrodischarge Machining Using Finite Element Method," Jpn. J. Appl. Phys., **44**, pp. 5254–5263.
[9] Yeo, S. H., Kurnia, W., and Tan, P. C., 2007, "Electro-Thermal Modelling of Anode and Cathode in Micro-EDM," J. Phys. D: Appl. Phys., **40**, pp. 2513–2521.
[10] Das, S., Koltz, M., and Klocke, F., 2003, "EDM Simulation: Finite Element-Based Calculation of Deformation, Microstructure and Residual Stress," J. Mater. Process Tech., **142**, pp. 434–451.
[11] Lasagni, A., Soldera, F., and Mucklich, F., 2004, "FEM Simulation of Local Heating and Melting During Electrical Discharge Plasma Impact," Modell. Simul. Mater. Sci. Eng., **12**, 835–844.
[12] Shervani-Tabar, M. T., Abdullah, A., and Shabgard, M. R., 2006 "Numerical Study on the Dynamics of an Electrical Discharge Generated Bubble in EDM," Eng. Anal. Boundary Elem., **30**, 503–514.
[13] Hockenberry, T. O., and Williams, E. M., 1976, "Dynamic Evolution of Events Accompanying the Low-Voltage Discharges Employed in EDM," IEEE. Trans. Ind. Appl., **IGA-3**, pp. 302–308.
[14] Klocke, F., Thomaidis, D., Garzon, M., Veselovac, D., and Klink, A., 2007, "Force Measurements in the Micro Spark Erosion With Various Electrode Materials, Polarities and Working Media," *Proceedings of 15th International Symposium on Electromachining* (*ISEM XV*, Pittsburgh), pp. 263–268.
[15] Eckman, P. K., and Williams, E. M., 1960 "Plasma Dynamics in an Arc Formed by Low-Voltage Sparkover of a Liquid Dielectric," Appl. Sci. Res. Sect. B, **8**, pp. 299–320.
[16] Tohi, M., Komatsu, T., and Kunieda, M., 2002 "Measurement of Process Reaction Force in EDM Using Hopkinson Bar Method," Int. J. Jpn. Soc. Precis. Eng. **68**, pp. 822–826 (in Japanese).
[17] FLUENT 6.3 User's Guide, Fluent Inc., 2006.
[18] Han, L., Liou, F. W., and Musti, S., 2005, "Thermal Behavior and Geometry Model of Melt Pool in Laser Material Process," Trans. ASME, J. Heat Transfer **127**, pp. 1005–1014.
[19] Childs, T. H. G., Hauser, G., and Badrossamay, M., 2005, "Selective Laser Sintering (Melting) of Stainless and Tool Steel Powders: Experiments and Modeling," Proc. Inst. Mech. Eng. Part B, **219**, pp. 339–357.
[20] Bayer, A. M., Vasco, T., and Walton, L. R., 1990, "Wrought Tool Steels, Properties and Selection: Irons, Steels, and High-Performance Alloys," *ASM Handbook*, ASM International, W. Materials Park, OH, Vol. 1, pp. 757–779.
[21] Kao, C. C., Tao, J., Shih, A. J., 2007, "Near Dry Electrical Discharge Machining," Int. J. Machine Tools Manuf., **47**, pp. 2273–2281.
[22] Li, Y. B., Lin, Z. Q., Chen, G. L., Wang, Y. S., and Xi, S. Y., 2002, "Study on Moving GTA Weld Pool in an Externally Applied Longitudinal Magnetic Field With Experimental and Finite Element Methods," Modell. Simul. Mater. Sci. Eng., **10**, pp. 781–798.
[23] Wong, Y. S., Rahman, M., Lim, H. S., Han, H., and Ravi, N., 2003, "Investigation of Micro-EDM Material Removal Characteristics Using Single RC-Pulse Discharges," J. Mater. Process Technol., **140**, pp. 303–307.
[24] Natsu, W., Shimoyamada, M., and Kunieda, M., 2006, "Study on Expansion Process of EDM Arc Plasma," JSME Int. J., Ser. C, **49**, pp. 600–605.
[25] Tao, J., Ni, J., and Shih, A. J., 2008, "Experimental Study of the Dry and Near-Dry Electrical Discharge Milling Processes," ASME J. Manuf. Sci. Eng., **130**(1), p. 011002.
[26] Reed-Hill, R. E., and Abbaschian, R., *Physical Metallurgy Principles*, PWS Publishing Company, Boston, MA, 1994, pp. 427–428.

Downloaded 11 Jan 2012 to 141.212.183.174. Redistribution subject to ASME license or copyright; see http://www.asme.org/terms/Terms_Use.cfm